

See discussions, stats, and author profiles for this publication at: <https://www.researchgate.net/publication/315349090>

Sedimentary basin exploration with receiver functions: Seismic structure and anisotropy of the Dublin Basin (Ireland)

Article in Geophysics · March 2017

DOI: 10.1190/geo2016-0471.1

CITATIONS

6

READS

266

2 authors:



Andrea Licciardi

Géoazur

23 PUBLICATIONS 56 CITATIONS

[SEE PROFILE](#)



Nicola Piana Agostinetti

University of Vienna

117 PUBLICATIONS 1,610 CITATIONS

[SEE PROFILE](#)

Some of the authors of this publication are also working on these related projects:



Multi-disciplinary Seismic Tomography [View project](#)



Seismic exploration with RF [View project](#)

Sedimentary basin exploration with receiver functions: Seismic structure and anisotropy of the Dublin Basin (Ireland)

Andrea Licciardi¹ and Nicola Piana Agostinetti²

ABSTRACT

Teleseismic receiver functions (RFs) were used to investigate the seismic structure of the southern margin of the Dublin Basin, a potential geothermal site. Through an inversion-based approach, the elastic properties and seismic anisotropy of sedimentary basin units were examined, using data from a linear array of closely spaced seismic stations. Our results were compared with sonic logs and lithostratigraphies from two nearby boreholes, NGE1 and NGE2 and colocated active seismic data. Including a high-frequency RF (up to 8 Hz) allowed us to compute S-wave velocity models with a vertical resolution <500 m. The results indicated the presence of a subvertical lateral discontinuity in V_S , in correspondence with the main basin-bounding fault (Blackrock-Newcastle Fault [BNF]). North of this discontinuity, a shallow low-velocity layer thickens (from 0.7 to 1.0 km thick) toward the inner basin, in agreement with the

geometry of the shallowest reflector found by active seismics. A good correlation was also found between the sonic log at NGE1 and our velocity model. Station DB02 showed an increase in V_S at a depth of approximately 0.7 km and a decrease in V_S at approximately 1.4 km in depth. Two velocity jumps with matching polarities were also observed in the NGE1 sonic log at the contact between the Upper and Lower Calp formations (positive jump, 688 m deep), and between a calcarenite and a sandstone layers (negative jump, 1337 m deep). Moreover, the main velocity contrasts in our model agree with the major lithostratigraphic boundaries inferred from borehole-drilled samples. Two juxtaposed anisotropic layers are identified close to the BNF. Directions of the slow axis of anisotropy are consistent with the borehole structural data. From these observations, the presence of aligned open cracks within the sandstones, possibly fluid-filled, was inferred up to a depth of 2.3 km in the vicinity of the BNF.

INTRODUCTION

The exploration of sedimentary basins for the earth's resources is usually driven by active seismics. The seismic properties of a target area (e.g., geothermal, CO₂ storage, gas, or oil reservoirs) are investigated through intense active seismic surveys. Although active seismic methods provide high-resolution images of the subsurface, they suffer from some limitations. First, strong and shallow reflectors or scattering may reduce the maximum depth of investigation preventing the successful imaging of deeper interfaces. Second, deep active seismics cannot be easily operated in a heavily populated environment. Third, the financial cost of an active seismic survey is quite substantial.

The receiver function (RF) method, a passive seismic technique, potentially overcomes these limitations and can offer an independent source of information to active seismics, although not at the same high resolution. In particular, RFs can be used to map the seismic structure of the subsurface in terms of S-wave velocity V_S . Depending on the resolution of the retrieved RF models, these could be used, in principle, to plan and design active seismic experiments and borehole drilling or to extend available single-point well seismic measurements of V_S to greater depths and on wider areas. Moreover, the RFs' sensitivity to contrast in anisotropic properties (Levin and Park, 1998; Savage, 1998; Luente et al., 2005; Shiomi and Park, 2008; Schulte-Pelkum and Mahan, 2014b; Audet, 2015; Bianchi et al., 2015) provides key information for the characterization of,

Manuscript received by the Editor 5 September 2016; revised manuscript received 22 February 2017; published online 9 May 2017.

¹Dublin Institute for Advanced Studies, Geophysics Section, School of Cosmic Physics, Dublin, Ireland and The University College Dublin, School of Geological Sciences, Belfield, Dublin, Ireland. E-mail: alicciardi@cp.dias.ie.

²Dublin Institute for Advanced Studies, Geophysics Section, School of Cosmic Physics, Dublin, Ireland. E-mail: piana@cp.dias.ie.

© 2017 Society of Exploration Geophysicists. All rights reserved.

e.g., a geothermal site, at which the identification of secondary porosity or fluids at depth plays a fundamental role.

The RF method (Langston, 1979; Ammon, 1991) represents a classic tool for the imaging of the earth's seismic structure. The P-to-S conversions contained in the P-coda of teleseismic earthquakes provide multifrequency information about the depth and amplitudes of impedance contrasts beneath a single seismic station. The vertical resolution of the method is frequency dependent. Because the teleseismic frequency peak is approximately 1 Hz, RFs have been classically applied to whole-crust and upper mantle imaging with vertical resolution of approximately 3–4 km. However, depending on the signal-to-noise ratio (S/N) at a given site, high-frequency RFs can also provide information about the structure of the shallow crust (0–5 km depth) (Leahy and Park, 2005; Zheng et al., 2005; Zevallos et al., 2009; Leahy et al., 2012).

Leahy et al. (2012) show that standard RF tools (used for crustal and upper mantle imaging) can be applied to high-frequency RF with little or no modification. For example, a classic approach to RF imaging involves stacking and migration of waveforms to produce 2D sections, which can be used to identify the presence of impedance contrasts at depth (for a review, see Rondenay, 2009). However, a velocity model needs to be assumed in most cases and, unless very sophisticated migration techniques are used, the retrieved images are blurred by the presence of multiples. This effect, especially when a thick sedimentary cover is present, can mask the real seismic structure (Clitheroe et al., 2000), making the interpretation nonunique. Another common RF method, known as $H\text{-}\kappa$ stacking (Zhu and Kanamori, 2000), is routinely used to determine bulk crustal thickness and V_P/V_S (e.g., Licciardi et al., 2014). This method can be adapted to estimate the depth of the basement in sedimentary basins (e.g., Leahy et al., 2012). Although very robust under a 1D approximation, this technique can produce misleading results in complex tectonic settings (where dipping interfaces and anisotropic bodies are expected) and in particular in potential geothermal areas, where the presence of fluid-related anisotropy can strongly affect the observed RFs (Hammond, 2014).

The aim of this work is to demonstrate the potential of up-to-date RF inversion methods to characterize the seismic structure and properties of the rocks in a sedimentary basin, in terms of seismic velocity and seismic anisotropy, comparing results from RF analysis with those from colocated active seismic and borehole data. To fulfill our goal, we analyze passive seismic data recorded across the southern border of the Dublin Basin (Ireland). The geothermal potential of the area, associated with the main basin-bounding fault (Blackrock-Newcastle Fault [BNF]), has attracted industry and academia interest in the past few years. For this reason, many geophysical surveys have been carried out across the area from 2008 to 2010, including active seismic profiles and pilot boreholes. To complement these geophysical data sets, we deployed six broadband seismic stations with an interstation distance of approximately 1 km, in a linear configuration normal to the BNF. Seismic stations recorded continuously for two years, and teleseismic data have been analyzed for computing RFs.

To exploit all the information contained in the RF data set, we adopt state of the art RF inversion-based techniques aimed to recover the isotropic (i.e., V_S variations in the subsurface) and 3D features (anisotropy and/or dipping interfaces) at depth. Throughout this analysis, we deal with a multifrequency RF data set (up to 8 Hz) to provide better constraints on absolute V_S values (Svenn

and Jacobsen, 2007). We show that inversion of RF can provide useful information in the context of sedimentary basin exploration and that our findings can be directly compared with the available borehole data. Our models provide insights into the structure and rock properties of the sedimentary units and into the state of fracturing and fault geometry of the area. Overall, our results can contribute to improve the understanding of geothermal potential in the Dublin Basin.

Geologic background and previous geophysical investigations

The Dublin Basin is a Carboniferous sedimentary basin, extending from the coast near Dublin to the Irish Midlands in central Ireland. In the Dublin area, the Dublin Basin shows an east–west-trending axis and is fault bounded on its northern and southern margins (Sevastopulo and Wyse, 2009). The study area is located between County Kildare and County Dublin in correspondence with the southern margin (Figure 1). Here, the BNF represents the main basin bounding fault and separates Lower Palaeozoic rocks from Late Devonian and Carboniferous sediments.

Marginal rocks are sedimentary rocks deformed during the Caledonian orogeny (Phillips et al., 1988). They show a major southwest–northeast structural trend, with the age increasing from east to west. The sedimentary succession north of the BNF is characterized by a thick sequence of limestones called the Calp formation (Strogen and Somerville, 1984), which are thought to be tightly folded (Hitzman, 1999). The origin of the BNF is related to the Caledonian orogeny, but its activity probably continued during the Carboniferous (Sevastopulo and Wyse, 2009). Hitzman (1999) proposes a reactivation of the BNF during Variscan compression that would have created the current, very-steep configuration of the fault plane. The BNF has been interpreted as a dextral shear zone, which probably involves a much more complex structural system than a single fault (Rothery and Phillips, 1983; Phillips et al., 1988).

The possible formation of dilation zones at depth (Phillips et al., 1988) along the BNF (with an associated increase in permeability and possible fluid circulation) has stimulated the interest for geothermal exploration in the area in recent years. Two relatively deep (reaching approximately 1.4 km depth) pilot boreholes, NGE1 and NGE2, have been drilled and seismic reflection profiles were acquired (Figure 1). The two boreholes crossed the Upper Calp limestones and shales and Lower Calp grainstone successions, without reaching the Lower Palaeozoic basement (Figure 1b). The NGE1 borehole crossed the bottom of the Calp formation, finding a thin calcarenite layer over a sandstone unit. A temperature of 46.2°C has been measured at the bottom of the borehole (1.4 km depth) with an estimated geothermal gradient of 32.38°C/km.

Available acoustic televiewer data from this borehole have shown the absence of major structural features in the first 650 m. These have also documented the presence of small-scale faulting at the top and bottom of the Lower Calp with modest fracturing throughout this sequence. The Lower Calp is characterized by an overall small dip (10°–40°) toward the southeast, which, however, presents high-frequency variations that suggest the presence of a fold. A major fault was encountered at a depth of 1337 m dipping southeast. Although no structural data are available below this depth, this fault is interpreted as a splay or a secondary fault of the BNF that contributes to create a high secondary porosity at the base of the sedimentary sequence (below the calcarenite layer), even at a significant

distance from the basin margin (~ 1 km). The sonic log acquired in the NGE1 borehole indicates an increase in V_P at the boundary between the Upper and Lower Calp and a decrease in V_P from the Lower Calp to the sandstone layer.

Active seismic data have been acquired with vibroseis sources and with geophones spaced 0.83 m along the line shown in Figure 1a. Along the resulting 2D migrated section, we interpret two main reflectors, at approximately 0.3 and 0.8 s two-way time (TWT), respectively, gently dipping toward the north (Figure 1c). The uppermost reflector is probably displaced by a fault at the southwest termination of the profile.

Despite the available information, a clear picture of the structural setting of the basin is still missing. In particular, the extent at the depth of the deformed and/or fractured area identified at NGE1 is yet unknown. This area has been ultimately identified as the main target for geothermal exploration in the Dublin Basin. Given the calculated geothermal gradient and the presence of highly porous rocks, the bottom part of the Carboniferous sediments has been targeted to deliver heat through a geothermal well doublet.

DATA AND METHODS

Data

Starting in July 2013, four broadband seismic stations equipped with a Guralp CMG-6TD sensor were deployed in a linear configuration across the southern margin of the Dublin Basin close to the village of Newcastle (Figure 1). The area is located in the proximity of high-rate communication roads, a small aerodrome and the Greenogue Business Park (a medium-sized industrial business park). One new station was added in March/April 2014 to extend the array toward the southwest (DB06). At the same time, due to logistic problems at the DB04 site, this station was redeployed in a new site (DB05) that is approximately 300 m away. Seismic data were collected with a sampling rate of 100 Hz with a recording period going from three months (DB04) to two years (DB01, DB02, and DB03). The array was designed to cross the main basin-bounding fault (BNF) almost perpendicularly and to be colocated as much as possible to previous geophysical surveys. With an interstation distance of approximately 1 km, this array provides the possibility of studying the short wavelength lateral variations in the structural setting of the shallow crust (0–5 km depth range).

Teleseismic data are analyzed as follows. First, a list of approximately 500 teleseismic events that occurred between July 2013 and September 2015, with magnitude greater than $M_W \geq 5.5$ and epicentral distance between 25° and 95° , is selected. For each station, only traces with a good S/N are retained after visual inspection of the waveforms. Then, after being downsampled to 25 Hz, the seismograms are rotated into the RTZ reference system, where R is the direction along the great circle path from the source to the

receiver, T is perpendicular to R in the horizontal plane, and Z is the vertical component. Inspection of the frequency content of the selected teleseismic data is shown in Figure S1 of the supplementary material. As noted by Leahy et al. (2012), although the mean S/N for frequencies ≥ 4 Hz is approximately 1, some individual events can still be used for high-frequency analysis.

At this stage, radial (R) and transverse (T) RFs are computed using the frequency-domain deconvolution method proposed by Di Bona (1998). Once RFs are obtained, another visual inspection is performed to retain only good-quality waveforms with small amplitude in the acausal part and little ringing. The computation and selection of the final RF data set is performed with four different choices of the Gaussian filter width (a parameter), which is used to low-pass the resulting RF. These values are $a = 2, 4, 8$, and 16, which correspond to a 90% frequency cut-off f_c of $\approx 1, 2, 4$, and 8 Hz, respectively. The range of frequencies considered in this work spans the classic one used in most of the RF studies, but this is extended to higher frequencies (8 Hz) to provide high resolution

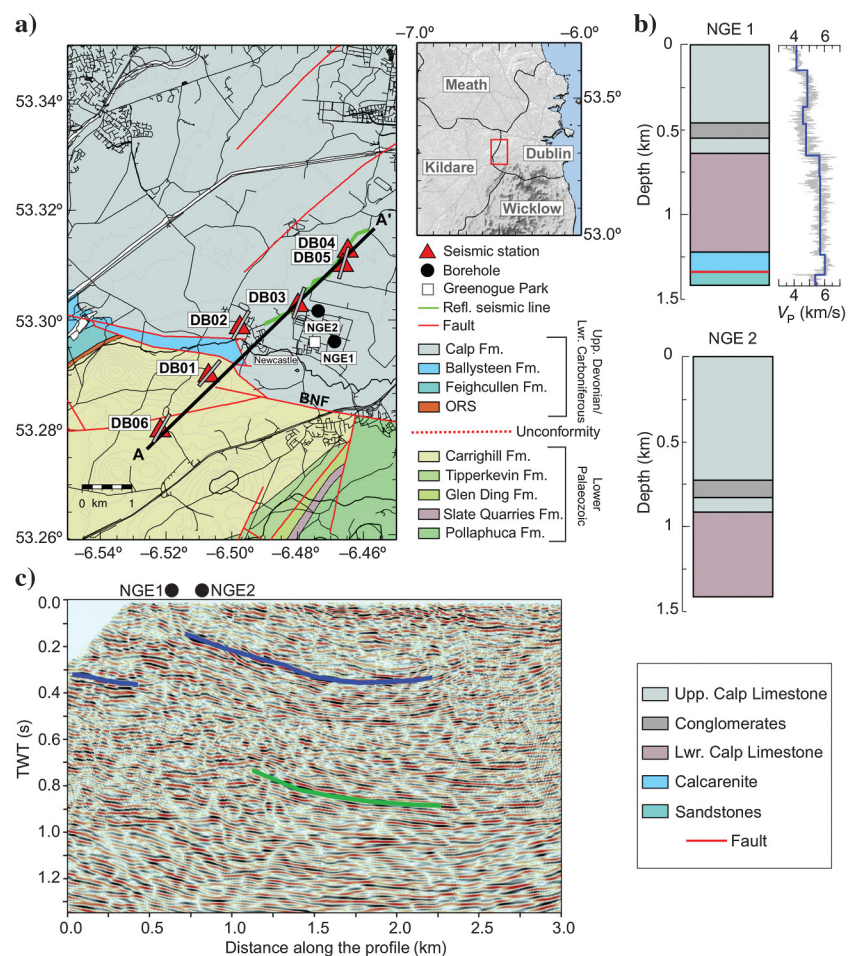


Figure 1. (a) Location of the seismic stations deployed in the Dublin Basin and geology map of the area. Gray bars indicate the strike of the fast plane for the shallowest layer retrieved from RF inversion. (b) Lithostratigraphies from boreholes NGE1 and NGE2 with the sonic log (gray line) and average interval velocities (blue line) from NGE1. The location of the boreholes is indicated in (a) with black circles. (c) Seismic reflection profile with interpretations of the main reflectors. The location of the profile is indicated with a green line in (a).

(<500 m) in the shallow crust. In the visual quality control of the highest frequency RF, particular attention has been paid to discarding waveforms with monochromatic components or with suspicious ringing. The final number of RFs at each station depends on the noise characteristics at each site and on the recording period. For our stations, this number varies from 12 at station DB04 to 47 at DB01. Except for station DB04, a fairly good azimuthal coverage is achieved (Figure 2).

A common practice in RF studies is to analyze the final RF data set as a function of the back azimuth after binning, to increase the S/N and assess the contribution of out-of-plane energy, hence the departure from the 1D assumptions. An example of such a back azimuthal sweep is shown in Figure 3 for station DB01. Binning is performed in back azimuth (20° bin width) and epicentral distance (40° bin width) with a 50% overlap. Epicentral distance bins are centered at 70° . If no RFs are found in this range, the adjacent bins are explored (gray numbers in Figure 3). In cases of isotropic and flat stratified media, all the energy should be confined in the R-RF whereas the T-RF should be zero. However, this is not the case for DB01 in which comparable amplitudes can be observed on both components. Coupled effects on the R- and T-RFs can be introduced by anisotropy and/or dipping velocity contrasts (Savage, 1998; Shiomi and Park, 2008). These effects are mainly observed as amplitude and delay time variations of the P_s pulses as a function of the back azimuth ϕ of the incoming P-wavefield with diagnostic two-lobed 2π and four-lobed π periodicities (Bianchi et al., 2010b).

Therefore, we can expect the presence of anisotropy and/or dipping interfaces beneath DB01.

Angular harmonic coefficients of RF data set

The aim of this study is to complement 1D isotropic profiles of S-wave velocity V_S with information about anisotropy and/or dipping velocity contrasts at depth. In the following, we use the term 3D features to indicate anisotropy and dipping structures, although all the analyses are performed in 1D.

In an RF data set, the effects induced by the isotropic structure and by the 3D features at depth are coupled to the R-RF and T-RF. To separate these effects, we apply the harmonic decomposition technique described in Bianchi et al. (2010b), to which the reader is referred for more details. The method is similar to the azimuthal filtering and stacking proposed by Girardin and Farra (1998) and Farra and Vinnik (2000). The RF data set is expanded in its back azimuthal harmonics for degree and order k assuming that it is composed of a combination of $\cos[k\phi(t)]$ and $\sin[k\phi(t)]$ terms. In this way, the azimuth-dependent features are isolated from the azimuth-invariant components. The $k = 0$ component (the azimuth-invariant component, also called the “constant” term) contains information about the depth and the amplitude of V_S contrasts. The $k = 1$ and 2 harmonics result from the sum of R-RF with T-RF, after a positive shift in the back azimuth ($+\pi/2k$) of the T-RF traces. This enhances the S/N and the two-lobed or four-lobed periodicity, respectively (Shiomi and Park, 2008). Two-lobed periodicity is associated with the presence of a dipping velocity contrast or anisotropy with a plunging symmetry axis at depth. Discriminating between these two possible sources of the two-lobed periodicity is not easy because they produce similar effects in the RF data set. However, the presence of polarity flips in the back azimuth on the T-RF at $t = 0$ s is diagnostic of dipping velocity contrasts and can be used to reduce the ambiguity (Audet, 2015). On the other hand, four-lobed periodicity is uniquely produced by anisotropy with a horizontal symmetry axis.

The effect of complex 3D structures, scattering, or incomplete geometric coverage can be quantified by performing the same stack with a negative phase shift ($-\pi/2k$, called “unmodeled” components hereinafter). Therefore, this quantity can be seen as an estimate of the error associated with the harmonic decomposition. In this work, we compute the terms of the first three orders ($k = 0, 1, 2$); however, because small amplitudes were found on the $k = 2$ harmonics compared to $k = 1$, we restricted the analysis only to the first-two-order harmonics. We display the components of $\cos[\phi(t)]$ and $\sin[\phi(t)]$ separately for $k = 1$, representing two normal directions (north–south and east–west) for a total of three harmonic coefficients (i.e., three time series), for each of the f_c considered.

An example of harmonic decomposition for station DB01 is displayed in Figure 4. A progressive increase in the frequency content of the analyzed RFs reveals more detail in the 0–2 s time range, in which most of the information about the structure of the upper crust is confined (e.g., primary and multiple conversions). The harmonic decomposition for the remaining stations (including $k = 2$ components) is shown in Figures S2–S7 of the supplementary material. Uncertainties on the computed $k = 0$ coefficients are estimated through a bootstrap analysis and resampling the original ensemble of high-quality RF. The results of the harmonic decomposition of the RF data set are used in a three-step approach to model the 1D isotropic structure and 3D features of the Dublin Basin.

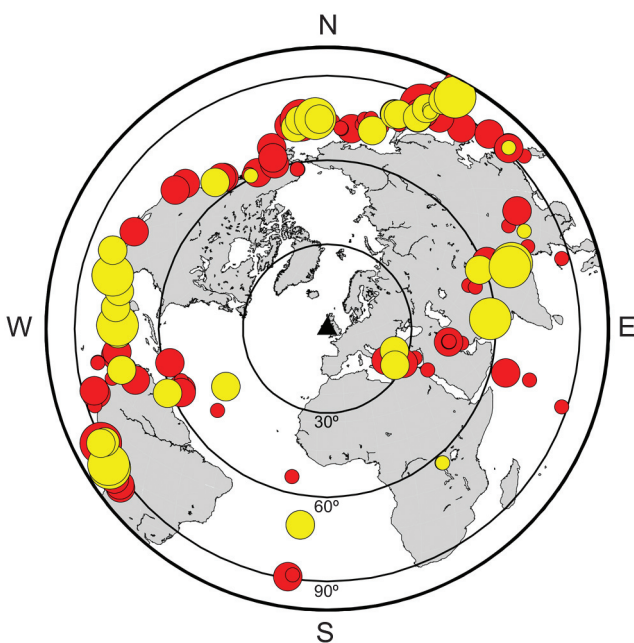


Figure 2. Azimuthal equidistant projection centered at station DB01 showing an example of the teleseismic earthquakes and RF data sets selection for two years. Events from 25° to 95° of epicentral distance have been visualized for the corresponding recording period. Red circles are the events selected after a visual inspection for which RFs were computed. Yellow circles represent the final set of high S/N RFs, used for further analysis. Circle size is proportional to the event magnitude.

1D isotropic inversion

The first step of our modeling procedure involves the inversion of RF waveforms to characterize the isotropic structure of the study area. RFs are mainly sensitive to the depth of impedance contrasts. To increase the sensitivity to absolute V_S values, we use a multifrequency approach following Svennigenen and Jacobsen (2007), inverting a few F isotropic components ($k = 0$ traces, one for each cut-off frequency considered). The RF inverse problem is nonlinear and non-unique (Ammon et al., 1990); therefore, inversion methods that provide a single best-fit solution (from linearized approaches to global optimization algorithms) usually fail to describe the complexity of the problem. Moreover, full uncertainty estimates on the retrieved parameters are difficult to obtain. We make use of a Bayesian approach to overcome these limitations. In Bayesian inference, prior knowledge about the model parameters (expressed in terms of probability distributions) is combined with information contained in the data (through the likelihood function), to produce a complex posterior probability distribution (PPD). This provides a natural way of incorporating statistics of the data errors in the inverse problem and map them into the final PPD, from which the nonuniqueness and robust uncertainties on model parameters, as well as correlation and trade-offs between them, can be quantified. The classic Bayesian framework can be expanded to infer directly from the data the complexity of the model, i.e., the number of parameters (transdimensional inversion; Green, 1995) and the magnitude of data noise (hierarchical approach; Malinverno and Briggs, 2004).

In this work, we make use of a reversible jump Markov chain Monte Carlo (rjMcMC) algorithm (Green, 1995) to sample the unknown target PPD. At the core of the algorithm, the Metropolis-Hastings rule (Metropolis et al., 1953; Hasting, 1970) drives the sampling according to the data and their error statistics (through the covariance matrix of data errors in the likelihood function). This means that the fit to the data is achieved in a statistical sense, and provided that data errors are correctly estimated, overfitting is avoided. We use the same implementation as Piana Agostinetti and Malinverno (2010), adjusting the likelihood to take multiple traces into account and inverting for the magnitude of data noise. We assume that the $k = 0$ waveforms to be inverted are independent between different frequencies. In other words, we assume that the ensembles of RFs used to compute the harmonics are made of independent observations among different f_c , for the same station. This assumption is generally satisfied, although, in practice, some overlap exists between different subsets of RFs. Nevertheless, by consid-

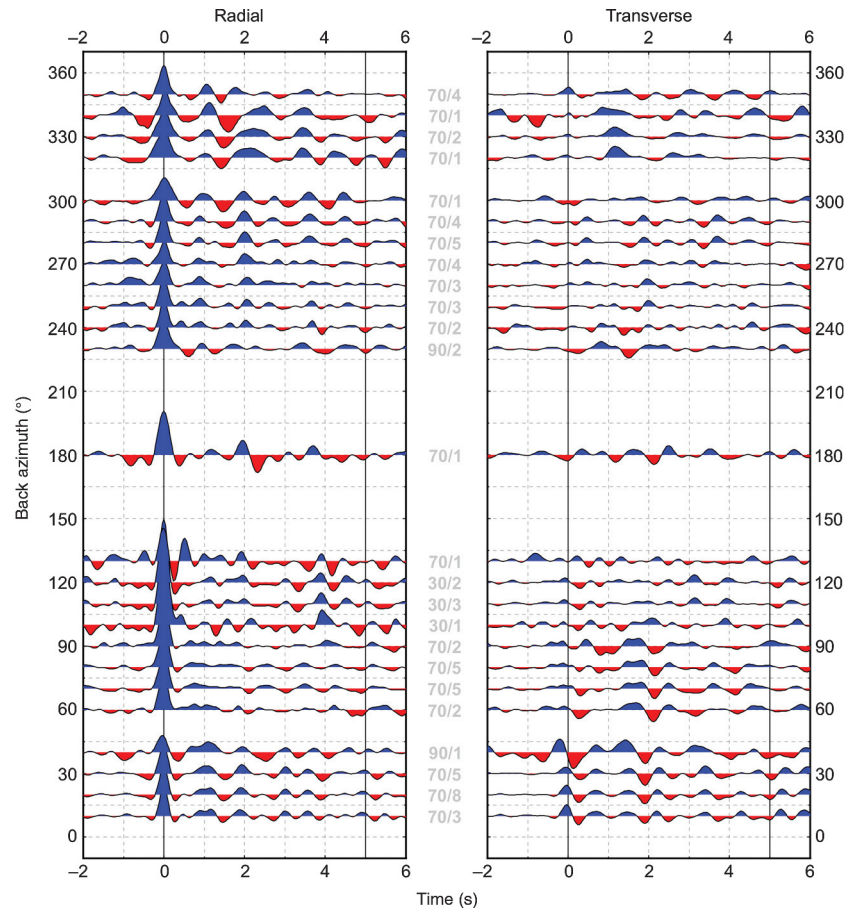


Figure 3. Binned radial and transverse RFs for station DB01, plotted as a function of back azimuth. Gray numbers indicate the central epicentral distance used in the binning procedure and the total number of RFs making up the bin, respectively.

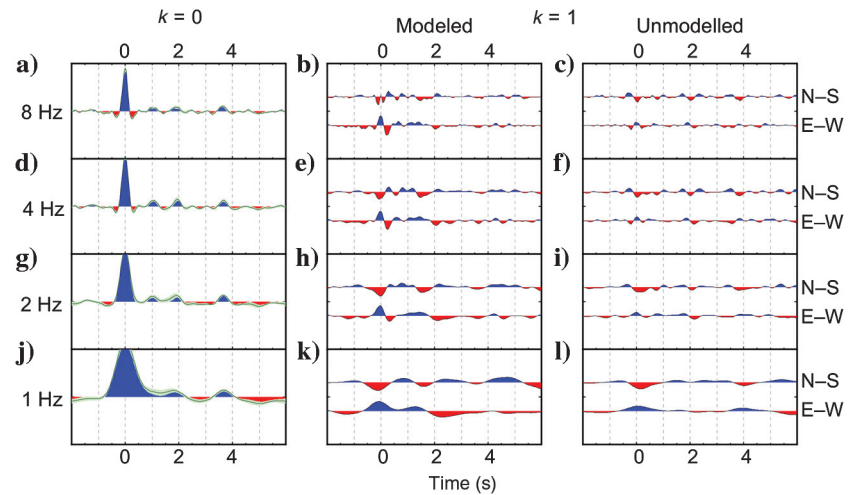


Figure 4. Harmonic decomposition analysis for station DB01. Data set in Figure 3 corresponds to the “4 Hz” panel. The first column contains the constant, zeroth-order harmonics ($k = 0$). The second and third columns show the $k = 1$ order harmonics corresponding to the summation of T and R with a positive ($+\pi/2$, “Aniso/dip”) and negative ($-\pi/2$, Unmodeled) shift in back azimuth, respectively. In each panel, the top trace is the $\cos \phi$ term and the bottom trace is the $\sin \phi$ term, corresponding to two normal directions (north-south and east-west). The green area around the $k = 0$ trace represents the standard deviation calculated with a bootstrap technique. The same amplitude scale is used in all plots.

ering independent $k = 0$ harmonics, the form of the likelihood function can be simply expressed as the product of F individual likelihoods:

$$p(\mathbf{d}|\mathbf{m}, \mathcal{I}) = \prod_{i=1}^F \frac{1}{[(2\pi)^N |h_i^2 \mathbf{C}_e^i|]^{1/2}} \exp \left[-\frac{1}{2} \mathbf{e}_i^T (h_i^2 \mathbf{C}_e^i)^{-1} \mathbf{e}_i \right], \quad (1)$$

where $\mathbf{e}_i = \mathbf{d}_i - g_i(\mathbf{m})$ is the difference between observed and predicted RF for a given model \mathbf{m} and \mathbf{C}_e^i is the covariance matrix of the data errors for the RF associated with the i th cut-off frequency. This matrix describes the statistics and correlation properties of the error on the observed data; N is the number of points in the inverted waveform.

We invert for the V_S , V_P/V_S , interface depths, number of interfaces, and magnitude of data noise through the hyperparameters h_i . Equation 1 shows how data error statistics contribute to the likelihood and, in turn, to the sampling of the PPD and its final shape. Here, the frequency-dependent correlation length is estimated with the empirical approach of Piana Agostinetti and Malinverno (2010) and our hierarchical approach mitigates the effect of wrong estimates of data errors. Moreover, each hyperparameter acts as a scaling factor for the whole covariance matrix and thus contributes to automatically weigh each RF differently in the inversion. Finally, by treating the number of parameters (the number of interfaces in our case) as an unknown in the inversion, the level of complexity (smoothness) of the solution is directly inferred from the data and their uncertainties; thus, no explicit regularization is needed. At the same time, the natural parsimony of transdimensional Bayesian inference prevents data from being overfit by very complex models: Given two models with a similar likelihood, the simpler one (e.g., the one with fewer interfaces) will be preferred (Malinverno, 2002).

Once the full PPD is obtained, marginal PPDs for the model parameters of interest (e.g., V_S and position of interface at depth) can be extracted from it and represent the main output of the algorithm. A posteriori uncertainties on the model parameters can be estimated from the output PPDs. These uncertainties contain con-

tributions from the noise in the data, approximations in the forward solver, and nonuniqueness of the inverse problem.

An example of such inversion for station DB01 is shown in Figure 5. The same results for the remaining stations are shown in Figure S8 of the supplementary material. We use 30 s long traces, and we set the maximum depth allowed for the interfaces to 60 km. The choice of inverting for the whole crust and uppermost mantle may appear counterintuitive when the focus of the work is mainly on the shallow crust. However, because multiple phases are also modeled by the forward solver, the risk of fitting a primary P_s phase as a multiple phase of an earlier arrival is strongly reduced.

In all our inversions, a priori information is set as follows. A Gaussian distribution with a depth-varying mean and standard deviation is used for V_S . Uniform distributions are chosen for the position of interfaces at depth (between 0 and 60 km, red line in Figure 5b) and for the number of layers (between 1 and 100, the red line in Figure 5d). For each station, we compute 100 parallel Markov chains with 8×10^5 models, discarding the first 4×10^5 models as part of the burn-in phase.

In our results, the Moho is clearly identified at approximately 32 km depth, on the marginal PPD of V_S (increase from 3.8 to 4.3 km/s) and of the position of interfaces at depth (Figure 5a and 5b). This result is in agreement with the crustal thickness estimated for Ireland (Landes et al., 2000; Licciardi et al., 2014). The Moho depth found is similar across all the stations, as expected for a dense array. A high degree of complexity is retrieved in the first 10 km of the crust, in terms of velocity variations and of the number of interfaces. Because this is the main target of this work, the following will focus only on the first 10 km of the crust when discussing the results of the rjMcMC inversion.

3D features at depth

Once the 1D isotropic structure beneath each station is obtained, this information can be used to constrain the presence of 3D features at depth. RF modeling of anisotropy and dipping interfaces is usually accomplished either by means of trial-and-error methods (Levin et al., 2002; Park et al., 2004; Savage et al., 2007; Liu et al., 2015) or

through fixed-dimension optimization schemes (Frederiksen et al., 2003; Ozacar and Zandt, 2009; Bianchi et al., 2010a, 2015; Roselli et al., 2010; Piana Agostinetti et al., 2011; Porter et al., 2011; Piana Agostinetti and Miller, 2014; Audet, 2015). The first approach is intrinsically user time consuming because many different models need to be tested. In the second case, the chosen parametrization can strongly influence the output models. To avoid these limitations, in the second step of our inversion analysis, we adopt the method described in Licciardi and Piana Agostinetti (2016), which is only briefly described here. This method automatically combines the information about the isotropic structure obtained from the rjMcMC inversion with the multifrequency $k = 1$ harmonics, to provide an optimum 1D parametrization (with uncertainties) that includes the position of 3D features at depth for a given station. This technique offers several advantages in RF modeling. First, the retrieved parametrization is directly inferred from the data and can be quickly

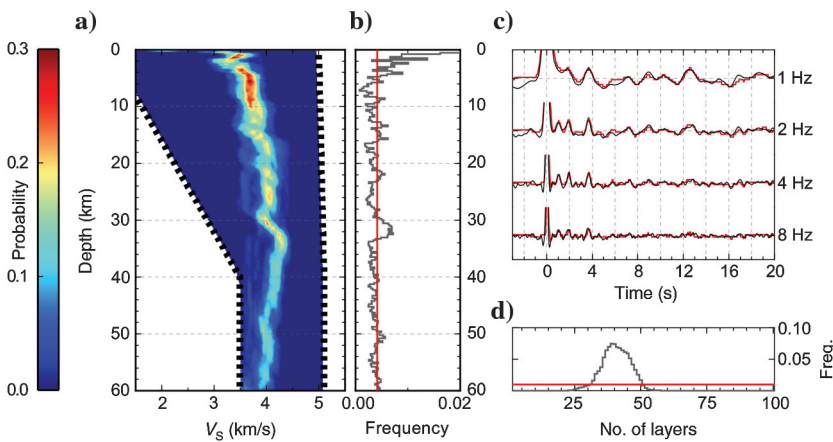


Figure 5. Results of the rjMcMC inversion for station DB01 for the whole crust. In (a and b), marginal PPDs of V_S and position of interfaces are shown. The fit between observed $k = 0$ harmonics (black lines) and a posteriori mean synthetics (red lines) is displayed in (c). The PPD for the number of interfaces is shown in (d). The red lines in (b and d) indicate the uniform prior level used in the inversion.

obtained without performing any inversions. Second, only one parameter (related to the estimated vertical resolution of the RF data set) has to be chosen by the user. Third, it allows us to exploit the resolving power of the RF data set through a multifrequency approach. As a result, the retrieved 1D parametrization can be used to guide a subsequent inversion for anisotropic parameters and interface geometry, reducing the overall nonuniqueness of the problem.

As an example, we show the application of this algorithm to station DB02 (Figure 6). The algorithm automatically extracts the depths of the main velocity discontinuities from the marginal PPDs of V_S and of the position of interfaces obtained through the rjMcMC inversion (Figure 6a). In practice, these discontinuities must fulfill two criteria: (1) They must correspond to a maximum on the marginal PPD for the position of interfaces, which has an amplitude above the uniform prior probability (the red line in the second and third panel), and (2) the absolute value of the velocity contrast across the interface must be larger than 0.1 km/s.

In a second step, the sum of the squares of the $\cos \phi$ and $\sin \phi$ components (called “energy” hereinafter) of the $k = 1$ harmonic is used as a proxy to locate the position of 3D features at depth (Figure 6b). By picking the maxima of this function (the red lines in Figure 6b) above the energy calculated for the unmodeled part (the blue lines), the algorithm identifies the depth of possible 3D discontinuities. This is done after time-to-depth conversion using the a posteriori mean V_S profile, extracted from the marginal PPD. Only coherent maxima between different frequencies are retained (red circles). The retrieved set of 3D discontinuities is joined to the set of main velocity discontinuities that fulfilled the two criteria set above, to produce a parametrization, which also provides constraints on the nature of the interfaces. For example, a dipping interface can produce a P_s arrival on the observed RFs only if a velocity jump is also present. For this reason, three different types of interface are possible in our approach: isotropic velocity jumps (blue interfaces), velocity jumps with associated variations in anisotropic properties and/or interface dip (green interfaces), and contrasts in anisotropic properties with no associated velocity jumps (red interfaces). The retrieved parametrization (Figure 6c) includes uncertainties on V_S (the 68% confidence interval computed from the PPD) and on the depth of interfaces.

In the last step of our modeling procedure, the parametrizations previously obtained are used to define a parameter space, which is explored by means of the neighborhood algorithm (NA; Sambridge, 1999). The NA relies on the properties of the Voronoi cell to guide an optimized search toward the region of lower misfit in the

model space. Two parameters need to be set in the NA inversion: the number of best-fitting cells to be resampled N_R and the number of samples generated for each cell at each iteration N_S . The ratio N_R/N_S controls the trade-off between exploration and exploitation of the model space. In our inversions, N_S is set to twice the number of investigated parameters and N_R/N_S is fixed to 0.1 as in Freder-

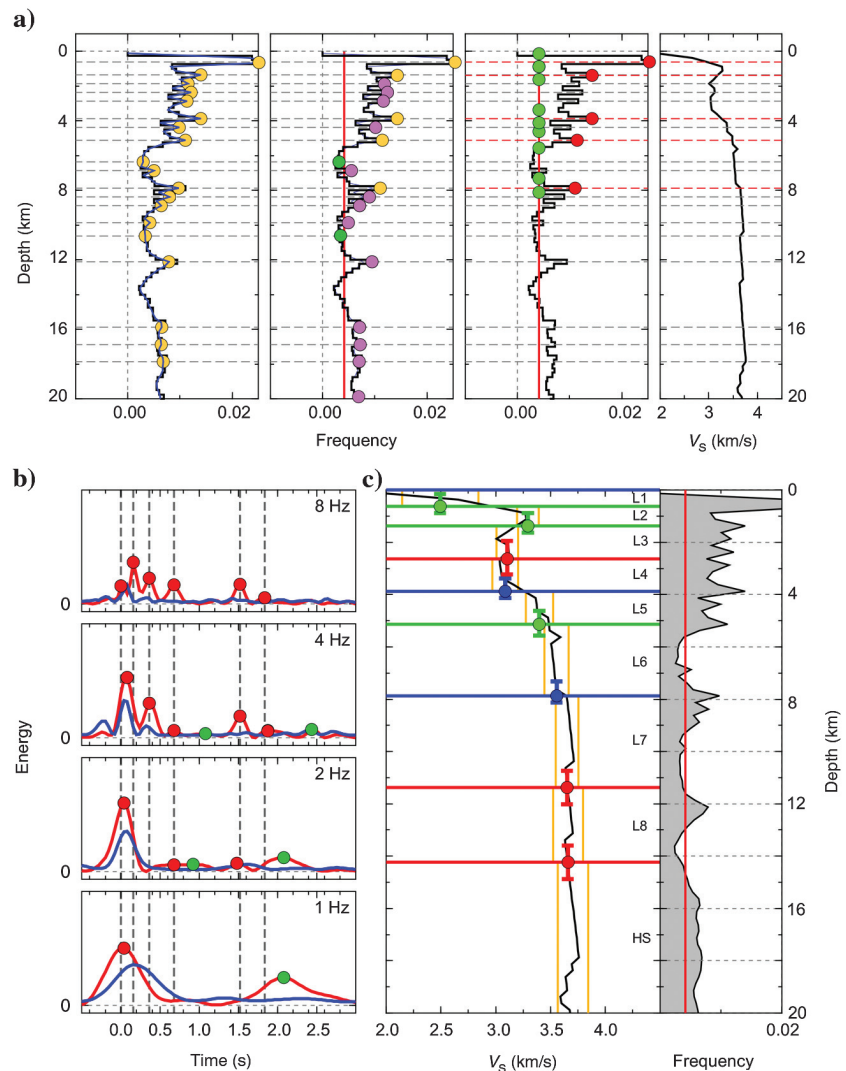


Figure 6. Results from the application of the automatic parametrization algorithm for station DB02. The automatic selection of isotropic and anisotropic interfaces is shown in (a and b), respectively. The final retrieved parametrization is displayed in (c). In (a), yellow circles are the maxima of the histogram of position of interfaces. Interfaces that do not match conditions (1) and (2) described in the main text are drawn with dark green and purple circles, respectively. Red circles are the final selected isotropic interface depths. Minimum and maximum values for the depth of each final selected interfaces are estimated from the width of the corresponding maximum (bright-green circles). In (b), energy on the $k = 1$ harmonics for the “modeled” (red lines) and unmodeled (blue lines) component for all the f_i considered. Circles are the maxima automatically picked on each trace. Only red circles are retained because these are present on consecutive frequencies. In (c), colored circles with error bars identify the depth of each interface and associated uncertainties. Blue lines are isotropic interfaces. Red lines are purely anisotropic interfaces, whereas green lines are anisotropic interfaces associated with an isotropic velocity jump. Yellow lines identify the mean 68% confidence interval for V_S . Black line is the mean V_S profile. On the right, the histogram of position of interfaces is plotted again for reference. See the text for details.

iksen et al. (2003). The misfit function, an l_2 -norm, is defined as the sum of the squares of the difference between observed and synthetic data. Synthetics are calculated with the forward solver RAYSUM (Frederiksen and Bostock, 2000) to model anisotropy and dipping interfaces from the observed RFs. The inversion is performed using the first 3 s of each RF that was used to compute the harmonics with a multifrequency approach. This time-window limits the maximum depth of the anisotropic or dipping layer to approximately 20 km, in agreement with our focus on the shallow crust. As a consequence,

our parameter space is limited to the discontinuities found in the first 20 km of the crust. Because little contribution is given by $f_i = 1$ Hz in detecting anisotropic interfaces in the shallow crust (see Figure 6b), this frequency is excluded from the inversion. For computational reasons, multiples are not included in the calculations of 3D synthetics.

For simplicity, we assume that all the energy on the $k = 1$ harmonics is due to anisotropy. Although the method of Licciardi and Piana Agostinetti (2016) provides robust constraints on the number and position of 3D features at depth, along with partial constraints on the nature of these discontinuities, some subjective choices are still required if one wants to model the anisotropic structure beneath the seismic station. As pointed out in Licciardi and Piana Agostinetti (2016), the method is not able to distinguish an anisotropic layer from an isotropic layer “sandwiched” between two anisotropic layers. However, the authors showed that the NA inversion resolves this ambiguity, producing a small amount of anisotropy for the latter case. For this reason, we only interpret layers with a considerable amount of anisotropy (i.e., >5%) and a plunge of the symmetry axis greater than 10°.

In the inversion, anisotropy is parametrized with a unique symmetry axis that can be either fast or slow, corresponding to positive or negative hexagonal anisotropy. The main source of anisotropy in the shallow crust is thought to be induced by alignment of open cracks, which produces negative anisotropy. Therefore, we assume the same amount of negative anisotropy for P- and S-wave velocities and we fix the parameter c of Levin and Park (1998) to zero (ellipsoidal velocity surfaces) (Sherrington et al., 2004; Bianchi et al., 2015). This choice is appropriate for cracked isotropic media (Hudson, 1981; Crampin, 1984). We invert for the trend (azimuth direction) and plunge (angle from the horizontal plane) of the symmetry axis, as well as for the intensity of anisotropy (defined as $2(v_{\max} - v_{\min}) / (v_{\max} + v_{\min})$, i.e., % peak-to-peak anisotropy) in each layer. The retrieved orientation of the slow symmetry axis of anisotropy can be used to define the strike and dip of the fast plane perpendicular to it, which would be the plane of orientation of microcracks or the plane of layering or foliation (Schulte-Pelkum and Mahan, 2014a, 2014b).

RESULTS

Isotropic structure

The results of the isotropic inversion for the first 10 km of the crust are shown in Figure 7 for all stations sorted from the southwest to northeast (from the margin to the inner basin). The fit between the modeled and observed data is generally good, with the only exception being station DB06, especially in the first second. Amplitudes

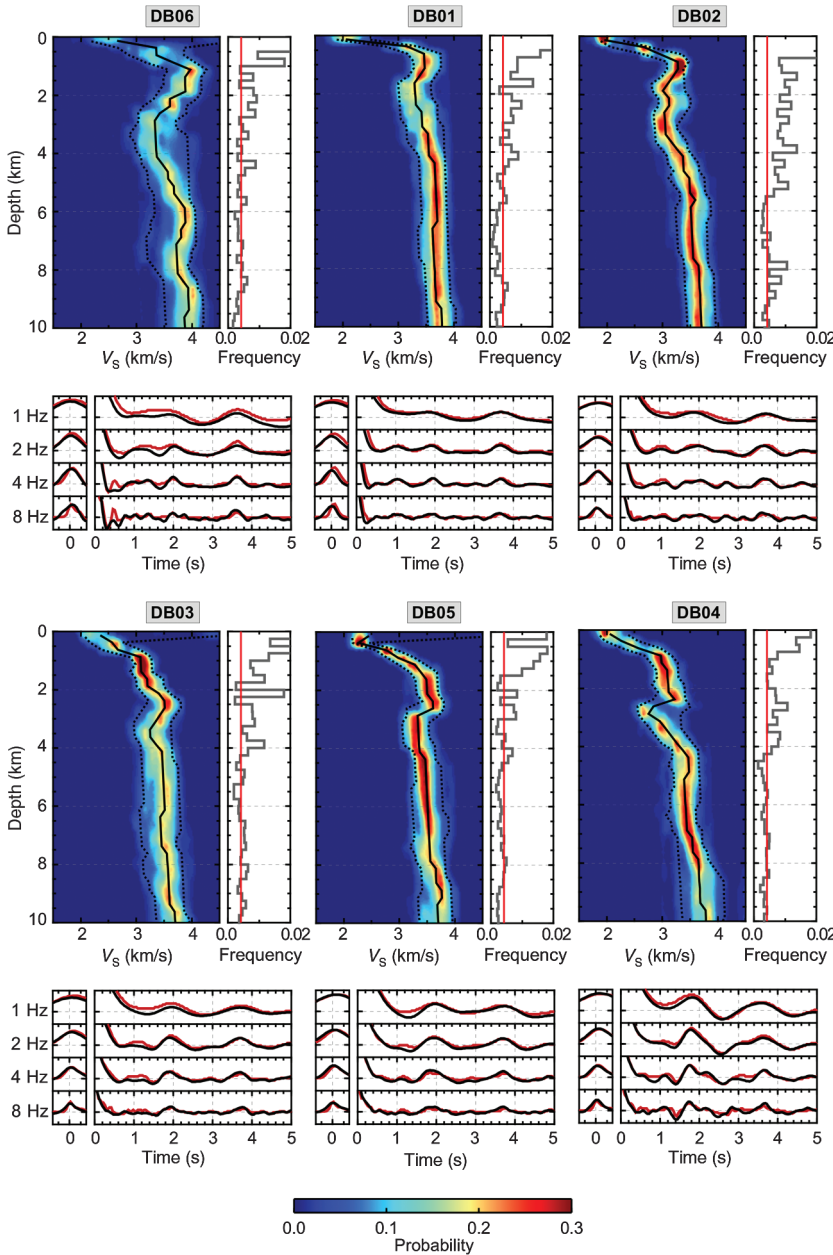


Figure 7. Results of the rjMcMC inversion for the first 10 km of the crust for all the stations of the DB array. For each station, the upper panels show the marginal PPD of V_S and the positions of the interfaces. The black solid line is the a posteriori mean, and dashed lines indicate the 95% confidence interval. In the bottom panels, the fit between observed (black traces) and mean a posteriori synthetics (red traces) are shown around the direct P-wave arrivals and in the first 5 s of the waveforms in two separate panels.

of the P-wave arrival at approximately 0 s are also well-reproduced by the synthetic waveforms. This is an important point because the amplitude of the direct-P pulse provides information on the S-wave velocity at progressively shallower depths as the RF frequency increases (Svenningsen and Jacobsen, 2007). Larger amplitudes are observed at 8 Hz for DB06 and DB01, which result in overall higher velocities in the first 2 km with respect to the remaining stations. The 95% confidence intervals on V_S are overall symmetric around the mean value with a width of approximately 0.5 km/s in this depth range. The histograms of position of interfaces at depth show the presence of multiple interfaces in the first 4 km, with DB02 being the most complex station.

To better understand lateral variations in S-wave velocity, we interpolate the mean V_S profiles computed from the marginal PPDs, along a vertical section running from southwest to northeast (Figure 8). The highest velocity at the surface ($V_S > 2.6$ km/s) is observed at DB06. Velocities as low as 2.0 km/s are found at the next two stations (DB01 and DB02), which are located on opposite sides of the BNF. Low velocities (between 2.0 and 2.4 km/s) are also observed for stations on the northern side of the BNF. Velocities of less than 3.0 km/s are found from 500 m to almost 1 km depth inside the basin, whereas at DB01, this transition is sharper, at approximately a 300 m depth. In the depth range of 1–4 km, a low-velocity zone (V_S less than 3.1 km/s) is found below station DB02. This seems to be in lateral continuity with DB03, at least between 1 and 2 km depth. However, on the south side of the BNF, velocities greater than 3.3 km/s are found below DB01 in the same depth range. This subvertical discontinuity correlates well with the surface position of the BNF. A zone of high velocities is found between 1 and 3 km depth below station DB05, which seems to extend under DB03 from 2 to 3 km depth. Finally, similar velocities of approximately 3.4–3.5 km/s are found for all stations at the bottom of the presented model. Strong lateral variations in V_S are found at depths greater than 1 km between DB05 and DB04. These stations are very close to each other, and they should sample similar rock volumes at depth. However, few RFs are available for station

DB04 due to the short recording period. Moreover, the poor back azimuthal distribution of events for this station can introduce a strong bias on the amplitudes of $k = 0$ harmonics and, thus, on the absolute V_S value at depth (see Figure 7). For these reasons, we consider the model at DB04 the less robust in terms V_S and therefore, we decide not to overinterpret the northeasternmost part of the retrieved 2D section. Nevertheless, the model at DB04 is deliberately included here to provide the reader with a broader picture of the RF potential (including possible limitations) for the imaging of the shallow crust.

Comparison with borehole data

In Figure 9, the results obtained with the rjMcMC inversion at stations DB02 and DB03 are compared with the available borehole data at NGE1 and NGE2. Results are displayed along a south–north-directed profile as indicated in the inset map of Figure 9. The depth reached by the boreholes is similar (approximately 1.4 km) and both provide constraints on the lithostratigraphy

of the sedimentary succession close to the north side of the BNF. In addition, P-sonic log data are available at NGE1. Although boreholes data provide much higher frequency information, the main features are coherent with the results of the rjMcMC inversion.

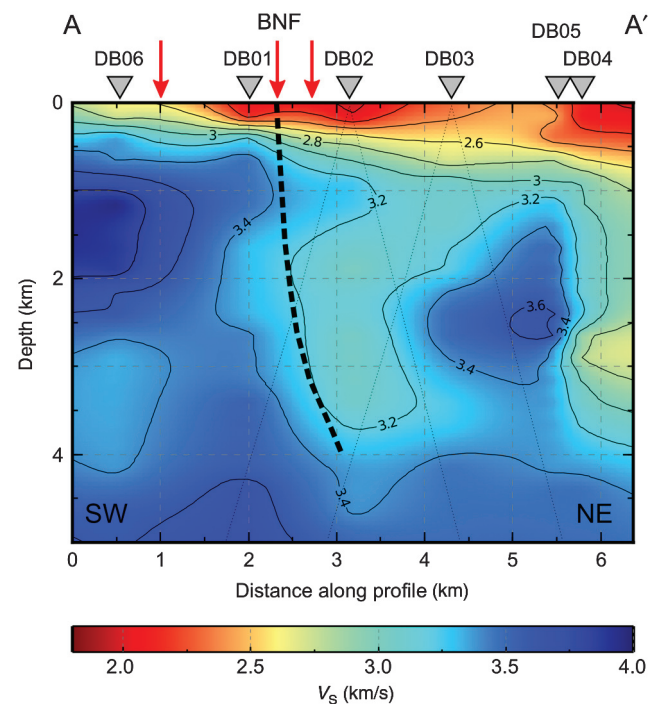


Figure 8. Depth distribution of V_S under the DB array. The a posteriori mean V_S profiles are interpolated along the section AA' of Figure 1. The position of the seismic station along the transect is shown with gray triangles, and red arrows mark the position of mapped fault at the surface. The black dashed line indicates the inferred position of the BNF at depth. Approximated station apertures for DB02 and DB03 are indicated with thin dashed lines.

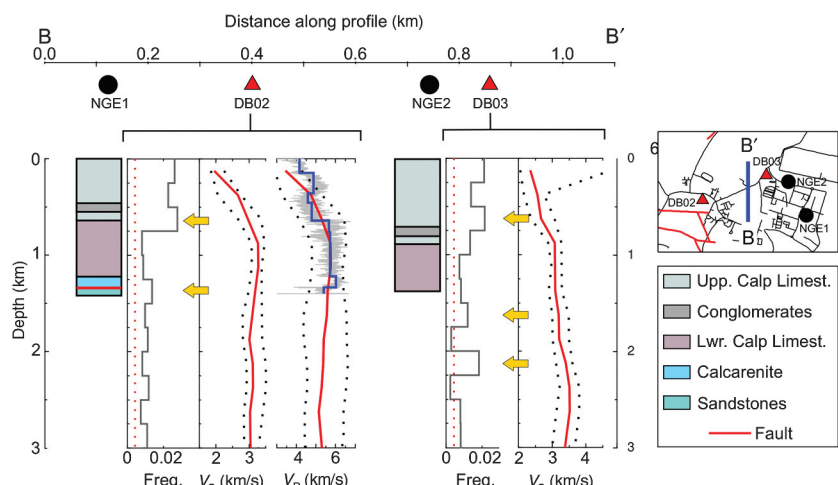


Figure 9. Comparison between the rjMcMC results at stations DB02 and DB03 with borehole data. The south–north-oriented section used to project the results is shown in the inset map. Position of stations and boreholes is indicated along the transect with red triangles and black circles, respectively. The PPDs of position of interfaces and V_S at depth are shown under the seismic stations. Yellow arrows indicate only the interfaces selected by the automatic algorithm. For DB02, sonic log data are shown in gray on the V_P panel. The blue profile is the average interval velocity profile.

Two main discontinuities are retrieved at DB02 (the yellow arrows in Figure 9) that correspond to positive and negative velocity jumps at ≈ 0.7 and ≈ 1.4 km, respectively. In between the two discontinuities, the histogram of the position of interfaces presents frequency values close to the a priori probability value, indicating the absence of any interface within such a depth range. These discontinuities correlate well with the lithologic boundaries between the Upper and Lower Calp and with the top of a sandstone layer found in the drilling records. Also, the sign of the velocity jumps across the two discontinuities is correctly retrieved when compared with the sonic log measurements. Most of the high-frequency variations in the first 700 m of the sonic log are not captured in our results, but the two main velocity jumps are well-recovered along with their position at depth. These observations imply a total thickness of approximately 0.7 km for the Lower Calp plus the calcarenite layer, in agreement with the 0.6 km found in the borehole. Also, the absence of any interface in between the retrieved main interfaces indicates the absence of S-velocity contrast between these two formations (whereas the sonic log presents a small, positive jump in P-velocity at such contact).

At DB03, only one interface is inferred from the results of the inversion in the depth range explored by borehole NGE2. The retrieved depth from the histogram of interfaces is approximately 700 m, but a higher velocity contrast is found a bit deeper in the marginal PPD of V_S (≈ 900 m). Again, this interface seems to correlate with the lithostratigraphic boundary between the Upper and Lower Calp, and the observed discrepancy of approximately 250 m for the location can be considered inside the error bounds of our method. Moreover, the histogram of the position of the interfaces displays the same pattern as seen at DB02 below the Upper-to-Lower Calp transition, i.e., the absence of any interface for approximately 500 m, suggesting the same thickness for the Lower Calp plus a calcarenite layer as in DB02. It is worth noticing that the V_S profile at DB03 does not present any velocity inversion below the Lower Calp unit.

In summary, the limit between the limestone of the Upper Calp and the grainstone of the Lower Calp gives rise to the main seismic feature in the first 1.5 km depth for both stations. This is seen as an increase in the S- and P-wave velocities. In particular, from the RF perspective, this limit is identified with the increase in V_S from less than to greater than 3.0 km/s.

Comparison with active seismic data

An active seismic survey has been carried out in the study area to investigate the continuity of the main seismic reflectors across the geothermal site. In particular, one seismic line was acquired parallel to the linear array of broadband seismic station used in this study. Unfortunately, such a seismic line does not extend out of the Dublin Basin, and thus, it does not cross the surface expression of the BNF (Figure 1a). In Figure 1c, we show the migrated active seismic image, together with our line drawing of the main reflectors. Such an image covers the northern portion of the profile shown in Figure 8 and continues for approximately 400 m to the north. Thus, the active seismic image can be approximately compared with the portion of V_S profile between stations DB03 and DB04. In such areas, the isovelocity contour at $V_S = 3.0$ km/s, defined above as the Upper-to-Lower Calp transition, seems to be almost flat at approximately 0.8 km depth. In the first 5–700 m from the free surface, the V_S profiles for DB03 and DB05 display different patterns (linear increase at

DB03, a relatively small velocity inversion at DB05) indicating more heterogeneous elastic structure in the first hundred meters at depth. These two observations roughly correlate with the line drawing presented in Figure 1c. In fact, the seismic reflector represented by the blue line in Figure 1c, which is interpreted as the top of the Lower Calp Grainstone, is found at approximately 0.3 s (TWT) at the two ends of the active seismic profile, where the two stations DB03 and DB05 have been deployed, depicting a flat horizon for the Upper-to-Lower Calp transition. Moreover, in the northern part of the profile, such seismic reflector marks the bottom of a region where very shallow high-reflectivity patches overlay an extended low-reflectivity area. Such a pattern is not found at the southern end of the profile, in agreement with the different “near-surface” (0–500 m depth) structure found at DB03 and DB05 stations, in the V_S profiles.

Anisotropic structure

The algorithm described in “3D features at depth” has been applied to obtain a 1D parametrization (with the location of 3D features) for each single station. For station DB02, such a parametrization is presented in Figure 6. The reader can find the results for the remaining stations in Figure S9 of the supplementary material. At station DB02, the parametrization comprises two anisotropic layers in the shallowest 3 km (marked as L2 and L3) and a deeper anisotropic layer in the middle crust (L8). Due to the presence of energy on the $k = 1$ harmonics at approximately 0.6 s, the possibility of having anisotropy within layers L4 and L5 cannot be excluded. Although some similarities in the parametrizations exist between adjacent stations, it is not easy to compare the results due to the different level of noise in the data. However, stations with high S/N (DB01, DB02, DB03, and DB05) show similar position of 3D features at depth. In particular, two anisotropic interfaces are found in the depth range between 11 and 16 km depth for all these stations, corresponding to L8 in Figure 6c.

The retrieved parametrizations are used to guide an inversion for anisotropic properties with the NA optimization scheme. In Figure 1a, we plot the results for the orientation of the fast plane, normal to the retrieved slow symmetry axis, for the shallowest anisotropic layer found at each station. The orientation of this plane is overall very similar between stations, striking southwest–northeast with small dip angles toward the southeast (10° – 30°).

Although we decided to model every 3D feature with anisotropy, the presence of dipping interfaces at depth cannot be excluded at stations DB01, DB04, DB05, and DB06. In this case, the strong energy on the $k = 1$ harmonics at $t = 0$ s could be related either to a superficial anisotropic layer or to a dipping velocity contrast at depth (Figure S9 of the supplementary material). On the other hand, stations DB02 and DB03 do not possess this feature, thus indicating that anisotropy is more likely to be the main source of the out-of-plane energy for these two stations. For this reason, in the following, we present and discuss the results of the NA inversion exclusively at stations DB02 and DB03, whereas the results for the remaining stations (except DB04 because of its poor azimuthal coverage) are shown in detail in Figure S10 of the supplementary material.

Anisotropic layers within the sedimentary basin: DB02 and DB03

In this section, we present the results of the NA inversion obtained by using the parametrization shown in Figure 6 and

Figure S9 (supplementary material), for stations DB02 and DB03, respectively. For DB02, the results of the inversion are shown in Figure 10 and in Table 1. Five possible anisotropic layers were identified by the automatic algorithm in the first 20 km of the crust (Figure 6c). However, after the inversion, two of these layers show a small amount of anisotropy (-2.6% in L4 + L5) and a small plunge of the symmetry axis ($\approx 4^\circ$ in L6 + L7). Therefore, we focus our attention on the remaining layers (L1, L2, and L8). In Figure 10, we show the distributions of anisotropic parameters for the models included in the best-fitting family (i.e., the ensemble of models which fit the observed wiggles with a misfit that is lower than the misfit of the best-fit model, increased by 10%). The best resolved parameter is usually the trend of the symmetry axis of anisotropy. Errors on intensity of anisotropy and on the plunge of the symmetry axis can be estimated to be roughly 4% and 10° , respectively. The fit between observed $k = 1$ harmonics and synthetic harmonics calculated for the best-fit model is good (Figure 10b), indicating that it captures the main anisotropic features at depth.

In Figure 11, the results are displayed as a function of depth (0–5 km) and compared with the stratigraphy observed at borehole NGE1. A significant amount of anisotropy is retrieved between 0.6 and 2.4 km depth in two distinct layers. The first anisotropic layer (L2 in Table 1 and Figure 10) is coherent in thickness and position with the Lower part of the Calp formation. It shows a strong amount of anisotropy ($\approx -16\%$) with the slow symmetry axis trending northwest and dipping with high angle ($\approx 75^\circ$). The second anisotropic layer shows weaker anisotropy, which is still significant ($\approx -8\%$) with the slow axis trending almost north and dipping with a similar high angle. The top of the second layer coincides with the negative velocity jump observed in the rjMcMC inversion, which, in turn, correlates with the top of the low-velocity sandstones found at NGE1. Moreover, this boundary is marked by the presence of a fault in the borehole. Structural data collected at NGE1 suggest that the fault is weakly dipping toward southeast. Between 2.4 and 4.8 km depth, a small amount of anisotropy is retrieved, indicating that this is probably an isotropic layer. However, the top of L6 was recognized as a 3D interface by the automatic algorithm. When modeled with anisotropy, this results in a layer with moderate anisotropy of approximately -6% , but with almost horizontal symmetry axis extending from 4.8 to almost 10 km. We do not exclude the possibility that this interface represents a dipping velocity contrast. In this case, it could be related to the presence of the BNF up to a depth of approximately 5 km. Between 10 and 13 km depth, L8 shows strong negative anisotropy (-11.5%) with the symmetry axis trending northwest and dipping at almost 30° . This is a robust feature found in consecutive stations with a good S/N (DB01, DB02, DB03, and DB05) as seen in

Figure S9 of the supplementary material. Anisotropic inversions for this layer show consistent results between these stations, with intensity of anisotropy varying between -10% and -12% , an almost unique trend of 330° , and plunge varying from 70° at DB01 to 20° – 30° for the remaining stations.

The results obtained for DB03 confirm the main findings for the shallow crust. In Figure 11, we show the NGE2 borehole lithostratigraphy compared with the anisotropic layering obtained by the NA algorithm for this station. The presence of a highly anisotropic layer between 0.7 and 2.0 km depth correlates with the Lower Calp, displaying the same trend and plunge found at station DB02 for such unit. However, at station DB03, the parametrization only includes one anisotropic layer in the shallow crust, in contrast with the two anisotropic layers found at station DB02 (see Figure S9 of

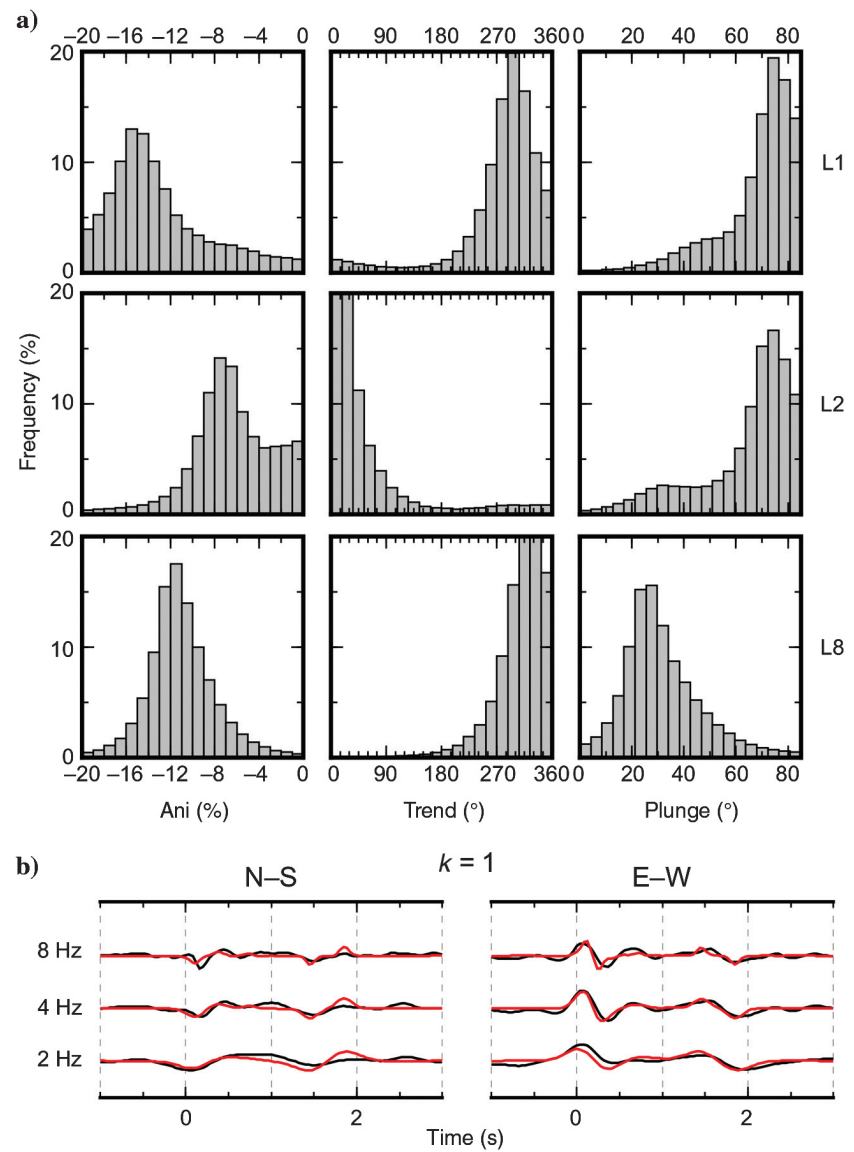


Figure 10. Results of the NA inversion at DB02. (a) Histograms of anisotropic parameters (intensity of anisotropy, trend, and plunge of the symmetry axis) for the best-fit family. (b) Fit between observed $k = 1$ harmonics and synthetic harmonics calculated for the best-fit model.

the supplementary material). The absence of such lower anisotropic layer matches the absence of the S-wave velocity inversion at station DB03, found at the base of the Lower Calp at station DB02, and suggests two competitive hypotheses: (a) the absence of the sandstone layer beneath station DB03 or (b) the absence of fluid-filled cracks within such layer at a greater distance from the BNF.

DISCUSSION

In the previous section, we presented the results of the analysis of RF data sets recorded across the southern border of the Dublin Basin, a carboniferous sedimentary basin. Our results have been compared with the local geophysical data, allowing to define where such results correlate with other independent observations. Here, we discuss the potential of RF analysis in the context of the exploration of the shallow crust, in terms of retrieving basin structures and mapping anisotropic volume within the basinal units. In particular, we focus on the possibility of using RF analysis for (a) defining the border of a sedimentary basin, following the main velocity contrast between basinal units and (b) defining the thickness and V_S of such units. We also discuss in detail the pros and cons of the RF methodology in retrieving the anisotropic properties of the sedimentary units within the basin.

Our RF analysis is carried out with a single-station approach. Therefore, the robustness of the captured lateral variations in the isotropic structure (Figure 8) and the anisotropic properties (Figure 1a and 11) is influenced by the station spacing. This parameter plays a fundamental role in designing any experiment, but it is subject to the trade-off between fieldwork logistics and the desired imaging target. In our case, the 1 km interstation distance does not allow overlapping rays in the first 2 km of the crust. Thus, in this depth range, interpretations about structural lateral variations should be considered with caution. Although some degree of speculation exists in our interpretation

of the isotropic structure, we decided not to overinterpret anisotropy and to limit the discussion to single-station observations.

As illustrated above, the transition from the sedimentary basin in the north to its border in the south can be recognized directly in the RF data from the amplitude of the direct-P pulse at the highest frequency (8 Hz). In fact, at such frequency, this value is related to the absolute value of the V_S in the 0–1 km depth range (Svennengen and Jacobsen, 2007). The results obtained with the rjMcMC inversion clearly confirm this observation. In our case, the velocity model for station DB06, which presents the maximum amplitude of the direct-P at 8 Hz, also shows near-surface V_S of approximately 2.7 km/s,

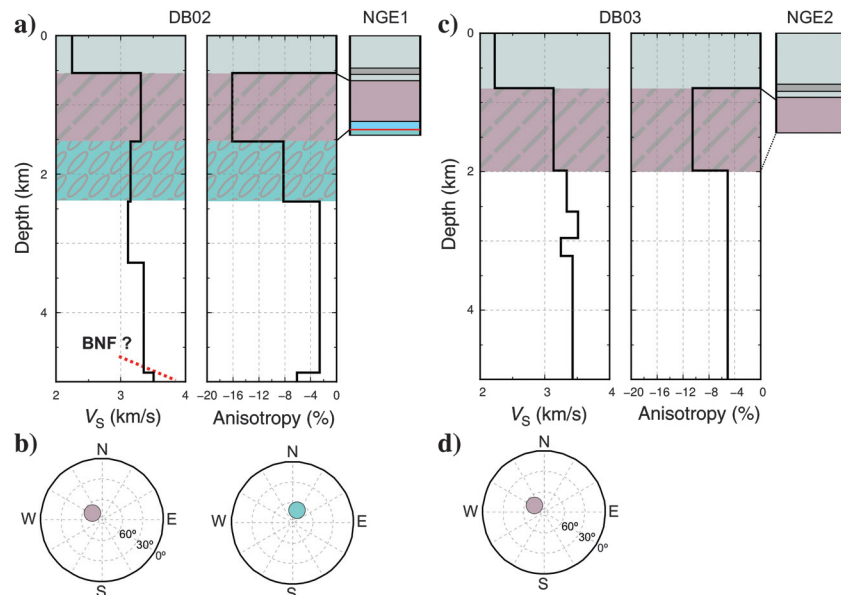


Figure 11. Results of the anisotropic inversion at stations DB02 and DB03 compared with lithostratigraphy at NGE1 and NGE2 wells. (a and b) S-wave velocity and anisotropy profiles at depth compared with borehole drilling results. Black lines in the profiles indicate the NA best-fit model. Patterns in the layers highlight the presence of significant anisotropy. (b and c) Orientation of the anisotropic symmetry axis on the lower hemisphere projection. Colors indicate geologic units as described in the legend of Figure 9. The inferred correlation between our results and lithostratigraphies from boreholes is indicated by the black lines.

Table 1. Parameter space boundaries and best-fit model in bold for station DB02; HS indicates the half-space, and the letter U means that the anisotropic parameters are the same as in the upper layer.

Layer	Thickness (km)	Density (kg cm^{-3})	V_S (km/s)	V_P/V_S	Ani P/S (%)	Trend (deg)	Plunge (deg)
1	0.2 / 0.9 (0.6)	2.6	2.1 / 2.8 (2.2)	1.78	0	0	0
2	0.25 / 1.0 (1.0)	2.6	3.2 / 3.4 (3.3)	1.75	-20/0 (-16.1)	0/360 (299)	0/85 (75)
3	0.2 / 2.0 (0.8)	2.6	3.0 / 3.2 (3.1)	1.74	-20/0 (-8.2)	0/360 (4)	0/85 (75)
4	0.75 / 1.5 (0.9)	2.6	3.0 / 3.2 (3.1)	1.74	-20/0 (-2.6)	0/360 (31)	0/85 (61)
5	0.75 / 1.7 (1.5)	2.6	3.3 / 3.5 (3.3)	1.76	U	U	U
6	2.2 / 3.0 (2.3)	2.6	3.5 / 3.6 (3.5)	1.82	-20/0 (-6.1)	0/360 (317)	0/85 (4)
7	2.8 / 4.2 (2.8)	2.6	3.5 / 3.7 (3.7)	1.82	U	U	U
8	2.1 / 3.5 (2.7)	2.6	3.5 / 3.7 (3.6)	1.77	-20/0 (-11.5)	0/360 (316)	0/85 (27)
HS		2.6	3.7 / 3.8 (3.7)	1.71	0	0	0

where all the other stations present $V_S < 2.6$ km/s at near-surface depths. In this view, we consider DB06 to be representative of the seismic structure of the basin margin, although this station shows higher uncertainties in the results (Figure 7). At a first glance, the striking difference between the velocity models for DB06 and DB01, at near-surface depth, could induce one to interpret the station DB01 as the last station (going southward) inside the sedimentary basin, also based on the similarity of the velocity in the 0–500 m depth range between DB01 and DB02. In doing so, an error as large as the interstation distance would be made. Based on surface geology, similar velocities observed at DB01 (south of the BNF) and DB02 (north of the BNF) in the first 500 m are not likely to represent the same geologic units. We argue that shallow intense faulting and fracturing around DB01 (see Figure 1) are the main causes of the observed low velocities. Summarizing, the geometry of the sedimentary basin, in terms of locating its bounding fault, can be assessed using RF analysis, with an error as small as the interstation distance. However, in presence of complex fault splays, the estimated error could be as large as twice such distance.

According to our results, the Upper portion of the Calp formation north of the BNF is defined as the shallowest layer with S-wave velocities < 3.0 km/s. This isovelocity contour line shows thickening from southwest to northeast from approximately 700 m at DB02 to almost 1 km at DB03 and DB05. This could reflect the original basin topography. In the portion of the profile where active and passive seismic data are available, the transition from Upper-to-Lower Calp is coherently retrieved in the two data sets (as an almost-horizontal reflector at 0.3 s TWT in the active seismics and as an almost horizontal isovelocity contour at approximately 1.0 km depth in the passive seismics). However, the active seismic data clearly depict fluctuations in the depth of this contact at a higher spatial frequency, which cannot be imaged using passive seismic data acquired with an interstation distance of approximately 1 km. Our findings confirm that the interstation distance is the limiting factor in recovering high-frequency lateral variations in the main seismic contacts within the basin.

The presence of the two boreholes drilled near our seismic profile allowed for a detailed comparison between the retrieved V_S velocity models and the well-log data (sonic log and lithostratigraphies). For station DB02, the depths of the main positive and negative velocity jumps are retrieved with an estimated error as small as the minimum allowed resolution (250 m). Moreover, the thickness of the Lower Calp formation is retrieved with a comparable resolution. In the second case, the contact between the Upper and Lower Calp is found with an error as small as 500 m. These results confirm that RF data contain information on short-wavelength fluctuations of the seismic velocity in the shallow crust (0–5 km depth) associated with a thin-layered (0.5 to 1.0 km thick) lithostratigraphy. Thinner layers could be theoretically imaged, if they present sharp velocity contrasts at the top and bottom interfaces (see DB05, Figure 8).

This work presents one of the first attempts to model anisotropy from RF data in the context of sedimentary basin exploration. One of the issues that can affect the interpretation of results is that physical sources of anisotropy are difficult to infer from RF data alone. It is generally believed that observed anisotropy in the first 5 km is the result of the coherent alignment of open cracks (possibly fluid filled), foliation of minerals, or simply stratification. The direction of the slow axis of anisotropy, as modeled in this work, is normal to the fast plane formed in the three cases. The orientation of this fast plane can be directly compared with borehole data and/or other available

information for a more robust interpretation of the RF results. In the study area, we found similar orientations of the fast plane for the shallowest anisotropic layer across the array. This orientation seems to be at an angle with the BNF (the major structural feature of the area) and could support the idea of this part of the Dublin Basin being a shear zone as proposed by Phillips et al. (1988). However, a similar effect could be simply due to the preexisting stratification geometry. Moreover, because differences in the outcropping rocks exist on the two sides of the BNF (from the lithologic and deformation history points of view), different sources of the observed anisotropy could coexist on the opposite sides of the BNF.

As a proof of concept, we discuss the results of anisotropic inversion at station DB02 alone because here the available borehole data can help to discriminate the physical source of the observed anisotropy. Structural data at NGE1 borehole indicate that a major fault dipping at low angle toward southeast is present at approximately 1.3 km depth. This has been interpreted as a splay or a secondary fault of the BNF. The orientation of the fault plane correlates well with the orientation of the slow symmetry axis that we found in the Lower Calp, which shows a high-angle plunge toward the northwest (Figure 11b). This is consistent with cracks that are oriented similarly to the fault plane. However, because modest fracturing has been observed in the rock samples collected during the drilling, our observed anisotropy could be simply related to the stratification within the unit. Borehole data report dips of strata toward southeast with small angles (10°–40°), which should produce a slow symmetry axis of apparent anisotropy trending on the opposite direction, with a complementary plunge. The second shallow anisotropic layer is less constrained by our results (Figure 10a), but it is very interesting for the geothermal perspective. Strongly fractured rocks with high secondary porosity and low V_P have been found at the base of the borehole NGE1 and have been related to the presence of the aforementioned fault. Our results suggest a slightly different orientation of the slow symmetry axis in this case (plunging at a high angle toward the north), but this could give an indication of the extent at depth of the fractured zone. If we assume that the observed anisotropy is related to fluid-filled cracks, this layer extends up at an approximately 2.3 km depth.

In the Dublin Basin, the main velocity contrast is located in the first 700 m, between the upper and lower parts of the Calp formation and does not exceed 1 km/s in the retrieved V_S models. We argue that this velocity contrast is not strong enough to produce a dominant chain of reverberations in the observed waveforms (see Figures 3 and S2–S7 in the supplementary material). It is worth noticing that, in other young sedimentary basins, the presence of very slow ($V_S < 0.5$ km/s) shallow sediments can generate a strong velocity contrast at the bottom of the basin, thus compromising the interpretation of classic migrated RF. Our inversion-based approach overcomes this limitation in principle because multiple phases are modeled in the RjMcMC isotropic inversion. On the other hand, to observe multiple phases generated by anisotropic contrasts, constant anisotropic properties over large distances are required. This is not usually the case. Even small variations in dip and the trend of the symmetry axis around the station can alter the azimuthal pattern of multiple phases, resulting in noncoherent stacking during the harmonic decomposition. For this reason, anisotropic multiples are difficult to observe on the $k = 1$ harmonics. This prevents our automated algorithm from adding apparent anisotropic layers in the final parametrization.

One of the strongest limitations in our NA inversion is deciding whether to use anisotropy or dipping interfaces to model the 3D features detected by our automated algorithm. This is especially true for very shallow interfaces. Nonetheless, the automatically retrieved parametrization can help to guide and interpret the NA inversion. In this work, for example, we made the a priori assumption that every 3D feature could be explained with anisotropy. By looking at the retrieved parametrizations, we recognized that for stations DB01, DB05, and DB06, this could be an oversimplification because dipping interfaces are probably the main cause of 3D effects, whereas for DB02 and DB03, anisotropy plays a major role. Prior geologic and/or geophysical information can help to reduce this ambiguity.

Another possible limitation of our approach to the optimization problem is related to how RFs with different frequencies are inverted together. In the rjMcMC isotropic inversion, the correct weights for each frequency are directly inferred from the data by means of different independent hyperparameters (see equation 1). On the other hand, in the NA inversion, equal weights for all frequencies are used and the simple misfit function based on L2 norm will bias the fit toward low frequencies. This could ultimately lead to an underutilization of the high-frequency component, likely resulting in an overestimation of the uncertainties on the retrieved anisotropic parameters. We acknowledge that our adopted inversion scheme is just one of the possible strategies to retrieve the anisotropic parameters or interface dip. A desirable improvement in methodology would be to make use of the Bayesian approach to invert for the 1D isotropic structure and anisotropy (and/or layer dip) at the same time. In this way, models with different structural features (e.g., isotropic versus anisotropic layer or dipping interfaces versus anisotropy) could be probabilistically compared and it would be possible to better quantify the associated non-uniqueness and uncertainties. Limitations to this development are mainly computational, and we believe that they will be overcome in the near future.

CONCLUSIONS

The results presented here show that inversion of RF for the characterization of the shallow crust can be used for basin exploration purposes. In particular, we believe that RF analysis can be used in the early stages of active seismic experiments to guide the planning and design of the surveys, or to complement active seismic and borehole information (e.g., velocity structure and anisotropy) at depth. Where controlled source techniques are impractical to operate, the RF method can provide a cheap alternative for the exploration of the subsurface.

We modeled isotropic and anisotropic properties of the shallow crustal rocks in the southern margin of the Dublin Basin. Our results correlate well with borehole data (lithostratigraphy and the P-wave sonic log), showing that, depending on the frequency used and the S/N, vertical resolution of up to 250 m can be obtained with teleseismic RF data. Also, comparison of our V_S model with active reflection seismic shows good correlation. Although reflection seismic data produce higher frequency images compared with teleseismic RF analysis, the lower frequency structural features of the inner basin are well-captured in our model. The BNF is identified as a major subvertical lateral V_S contrast in the proximity of the basin margin. We interpret a shallow low-velocity layer north of the BNF as the limestone of the Upper Calp. Its thickness increases from approximately 700 m to almost 1 km from the southwest to northeast inside the basin. Results from anisotropic inversions have been presented as

a proof of concept for the applicability of the RF method for sedimentary basin exploration.

In the proximity of the BNF, two consecutive anisotropic layers with slightly different orientations of the symmetry axis have been recognized. These orientations are coherent with the structural data from the NGE1 borehole. In particular, they agree with the orientation of a secondary fault of the BNF observed at NGE1. Although the source of anisotropy cannot be uniquely constrained by RF data, we attribute the observed anisotropy to layering and/or to the presence of aligned cracks at depth, possibly fluid filled. In more detail, we correlate the zone of high secondary porosity encountered at the bottom of the borehole NGE1 (at approximately 1.35 km depth) with the deeper of the two anisotropic layers associated with a decrease in S-wave velocity and fluid-filled aligned cracks. The extent of this zone is inferred to reach a depth of 2.3 km. This provides additional information in the context of the geothermal potential assessment of the area.

ACKNOWLEDGMENTS

We thank the associate editor J. Shragge, G. Leahy, and four anonymous reviewers for their suggestions and comments, which helped to strongly improve the quality of the manuscript. We are profoundly grateful to GTEnergy and R. Pasquali for sharing the reflection and boreholes data. A. Licciardi would like to thank J. Vozár for his support and for fruitful discussions. This publication has emanated from research conducted with the financial support of Science Foundation Ireland & the Marie-Curie Action COFUND under grant number 11/SIRG/E2174. The authors wish to acknowledge the DJEI/DES/SFI/HEA Irish Centre for High-End Computing for the provision of computational facilities and support. Figures were prepared using the generic mapping tool of [Wessel and Smith \(1998\)](#).

REFERENCES

- Ammon, C. J., 1991, The isolation of receiver effects from teleseismic P waveforms: *Bulletin of the Seismological Society of America*, **81**, 2504–2510.
- Ammon, C. J., G. E. Randall, and G. Zandt, 1990, On the non-uniqueness of receiver function inversions: *Journal of Geophysical Research*, **95**, 15303–15318, doi: [10.1029/JB095iB10p15303](https://doi.org/10.1029/JB095iB10p15303).
- Audet, P., 2015, Layered crustal anisotropy around the San Andreas Fault near Parkfield, California: *Journal of Geophysical Research: Solid Earth*, **120**, 1–17.
- Bianchi, I., G. Bokelmann, and K. Shiomi, 2015, Crustal anisotropy across northern Japan: *Journal of Geophysical Research: Solid Earth*, **120**, 4998–5012.
- Bianchi, I., C. Chiarabba, and N. Piana Agostinetti, 2010a, Control of the 2009 L’Aquila earthquake, central Italy, by a high-velocity structure: A receiver function study: *Journal of Geophysical Research*, **115**, B12326, doi: [10.1029/2009JB007087](https://doi.org/10.1029/2009JB007087).
- Bianchi, I., J. Park, N. Piana Agostinetti, and V. Levin, 2010b, Mapping seismic anisotropy using harmonic decomposition of receiver functions: An application to Northern Apennines, Italy: *Journal of Geophysical Research*, **115**, B12317, doi: [10.1029/2009JB007061](https://doi.org/10.1029/2009JB007061).
- Clitheroe, G., O. Gudmundsson, and B. L. N. Kennett, 2000, Sedimentary and upper crustal structure of Australia from receiver functions: *Australian Journal of Earth Sciences*, **47**, 209–216, doi: [10.1046/j.1440-0952.2000.00774.x](https://doi.org/10.1046/j.1440-0952.2000.00774.x).
- Crampin, S., 1984, Effective elastic constants for wave propagation through cracked solids: *Geophysical Journal of the Royal Astronomical Society*, **76**, 135–145, doi: [10.1111/j.1365-246X.1984.tb05029.x](https://doi.org/10.1111/j.1365-246X.1984.tb05029.x).
- Di Bona, M., 1998, Variance estimate in frequency-domain deconvolution for teleseismic receiver function computation: *Geophysical Journal International*, **134**, 634–646, doi: [10.1111/j.1365-246X.1998.tb07128.x](https://doi.org/10.1111/j.1365-246X.1998.tb07128.x).
- Farra, V., and L. Vinnik, 2000, Upper mantle stratification by P and S receiver functions: *Geophysical Journal International*, **141**, 699–712, doi: [10.1046/j.1365-246x.2000.00118.x](https://doi.org/10.1046/j.1365-246x.2000.00118.x).

- Frederiksen, A. W., and M. G. Bostock, 2000, Modeling teleseismic waves in dipping anisotropic structures: *Geophysical Journal International*, **141**, 401–412, doi: [10.1046/j.1365-246x.2000.00090.x](https://doi.org/10.1046/j.1365-246x.2000.00090.x).
- Frederiksen, A. W., H. Folsom, and G. Zandt, 2003, Neighbourhood inversion of teleseismic Ps conversions for anisotropy and layer dip: *Geophysical Journal International*, **155**, 200–212, doi: [10.1046/j.1365-246X.2003.02043.x](https://doi.org/10.1046/j.1365-246X.2003.02043.x).
- Girardin, N., and V. Farr, 1998, Azimuthal anisotropy in the upper mantle from observation of P-to-S converted phases: Application to southeast Australia: *Geophysical Journal International*, **133**, 615–629, doi: [10.1046/j.1365-246X.1998.00525.x](https://doi.org/10.1046/j.1365-246X.1998.00525.x).
- Green, P. J., 1995, Reversible jump Markov chain Monte Carlo computation and Bayesian model determination: *Biometrika*, **82**, 711–732, doi: [10.1093/biomet/82.4.711](https://doi.org/10.1093/biomet/82.4.711).
- Hammond, J., 2014, Constraining melt geometries beneath the Afar Depression, Ethiopia from teleseismic receiver functions: The anisotropic h-k stacking technique: *Geochemistry, Geophysics, Geosystems*, **15**, 1316–1332, doi: [10.1002/ggge.v15.4](https://doi.org/10.1002/ggge.v15.4).
- Hastings, W. K., 1970, Monte Carlo sampling methods using Markov chains and their applications: *Biometrika*, **57**, 97–109, doi: [10.1093/biomet/57.1.97](https://doi.org/10.1093/biomet/57.1.97).
- Hitzman, M. W., 1999, Extensional faults that localize Irish syndiagenetic Zn-Pb Deposits and their reactivation during Variscan compression, in *Fractures, Fluid Flow and Mineralization*: Geological Society, London, Special Publications 155, 233–245.
- Hudson, J., 1981, Wave speeds and attenuation of elastic waves in material containing cracks: *Geophysical Journal of the Royal Astronomical Society*, **64**, 133–150, doi: [10.1111/j.1365-246X.1981.tb02662.x](https://doi.org/10.1111/j.1365-246X.1981.tb02662.x).
- Landes, M., C. Prodehl, F. Hauser, A. W. B. Jacob, and N. J. Vermeulen, 2000, VARNET-96: Influence of the Variscan and Caledonian orogenies on crustal structure in SW Ireland: *Geophysical Journal International*, **140**, 660–676, doi: [10.1046/j.1365-246X.2000.00035.x](https://doi.org/10.1046/j.1365-246X.2000.00035.x).
- Langston, C. A., 1979, Structure of the Mount Rainier, Washington, inferred from teleseismic body waves: *Journal of Geophysical Research*, **84**, 4749–4762, doi: [10.1029/JB084iB09p04749](https://doi.org/10.1029/JB084iB09p04749).
- Leahy, G. M., and J. Park, 2005, Hunting for oceanic island Moho: *Geophysical Journal International*, **160**, 1020–1026, doi: [10.1111/j.1365-246X.2005.02562.x](https://doi.org/10.1111/j.1365-246X.2005.02562.x).
- Leahy, G. M., R. L. Saltzer, and J. Schmedes, 2012, Imaging the shallow crust with teleseismic receiver functions: *Geophysical Journal International*, **191**, 627–636, doi: [10.1111/j.1365-246X.2012.05615.x](https://doi.org/10.1111/j.1365-246X.2012.05615.x).
- Levin, V., and J. Park, 1998, P-SH conversions in layered media with hexagonally symmetric anisotropy: A cookbook: *Pure and Applied Geophysics*, **151**, 669–697, doi: [10.1007/s00240050136](https://doi.org/10.1007/s00240050136).
- Levin, V., J. Park, M. Brandon, J. Lees, V. Peyton, E. Gordeev, and A. Ozerov, 2002, Crust and upper mantle of Kamchatka from teleseismic receiver functions: *Tectonophysics*, **358**, 233–265, doi: [10.1016/S0040-1951\(02\)00426-2](https://doi.org/10.1016/S0040-1951(02)00426-2).
- Licciardi, A., and N. Piana Agostinetti, 2016, A semi-automated method for the detection of seismic anisotropy at depth via receiver function analysis: *Geophysical Journal International*, **205**, 1589–1612, doi: [10.1093/gji/ggw091](https://doi.org/10.1093/gji/ggw091).
- Licciardi, A., N. Piana Agostinetti, S. Lebedev, A. J. Schaeffer, P. W. Readman, and C. Horan, 2014, Moho depth and Vp/Vs in Ireland from teleseismic receiver functions analysis: *Geophysical Journal International*, **199**, 561–579, doi: [10.1093/gji/ggu277](https://doi.org/10.1093/gji/ggu277).
- Liu, Z., J. Park, and D. M. Rye, 2015, Crustal anisotropy in northeastern Tibetan Plateau inferred from receiver functions: Rock textures caused by metamorphic fluids and lower crust flow?: *Tectonophysics*, **661**, 66–80, doi: [10.1016/j.tecto.2015.08.006](https://doi.org/10.1016/j.tecto.2015.08.006).
- Lucente, F. P., N. Piana Agostinetti, M. Moro, G. Selvaggi, and M. Di Bona, 2005, Possible fault plane in a seismic gap area of the southern Apennines (Italy) revealed by receiver function analysis: *Geophysical Journal International*, **110**, B04307.
- Malinverno, A., 2002, Parsimonious Bayesian Markov chain Monte Carlo inversion in a nonlinear geophysical problem: *Geophysical Journal International*, **151**, 675–688, doi: [10.1046/j.1365-246X.2002.01847.x](https://doi.org/10.1046/j.1365-246X.2002.01847.x).
- Malinverno, A., and V. A. Briggs, 2004, Expanded uncertainty quantification in inverse problems: Hierarchical Bayes and empirical Bayes: *Geophysics*, **69**, 1005–1016, doi: [10.1190/1.1778243](https://doi.org/10.1190/1.1778243).
- Metropolis, N., A. W. Rosenbluth, N. M. Rosenbluth, A. H. Teller, and E. Teller, 1953, Equation of state calculations by fast computing machines: *The Journal of Chemical Physics*, **21**, 1087–1092, doi: [10.1063/1.1699114](https://doi.org/10.1063/1.1699114).
- Ozacar, A. A., and G. Zandt, 2009, Crustal structure and seismic anisotropy near the San Andreas Fault at Parkfield, California: *Geophysical Journal International*, **178**, 1098–1104, doi: [10.1111/j.1365-246X.2009.04198.x](https://doi.org/10.1111/j.1365-246X.2009.04198.x).
- Park, J., H. Yuan, and V. Levin, 2004, Subduction zone anisotropy beneath Corvallis, Oregon: A serpentinite skid mark of trench-parallel terrane migration?: *Journal of Geophysical Research*, **109**, B10306, doi: [10.1029/2003JB002718](https://doi.org/10.1029/2003JB002718).
- Phillips, W., A. Rowlands, D. Collier, J. Carter, and A. Vaughan, 1988, Structural studies and multidata correlation of mineralization in central Ireland, in *Mineral Deposit within the European Community*: Springer-Verlag, 353–377.
- Piana Agostinetti, N., I. Bianchi, A. Amato, and C. Chiarabba, 2011, Fluid migration in continental subduction: The Northern Apennines case study: *Earth and Planetary Science Letters*, **302**, 267–278, doi: [10.1016/j.epsl.2010.10.039](https://doi.org/10.1016/j.epsl.2010.10.039).
- Piana Agostinetti, N., and A. Malinverno, 2010, Receiver function inversion by trans-dimensional Monte Carlo sampling: *Geophysical Journal International*, **181**, 858–872.
- Piana Agostinetti, N., and M. S. Miller, 2014, The fate of the downgoing oceanic plate: Insight from the Northern Cascadia subduction zone: *Earth and Planetary Science Letters*, **408**, 237–251, doi: [10.1016/j.epsl.2014.10.016](https://doi.org/10.1016/j.epsl.2014.10.016).
- Porter, R., G. Zandt, and N. McQuarrie, 2011, Pervasive lower-crustal seismic anisotropy in southern California: Evidence for underplated schists and active tectonics: *Lithosphere*, **3**, 201–220, doi: [10.1130/L126.1](https://doi.org/10.1130/L126.1).
- Rondenay, S., 2009, Upper mantle imaging with array recordings of converted and scattered teleseismic waves: *Surveys in Geophysics*, **30**, 377–405, doi: [10.1007/s10712-009-9071-5](https://doi.org/10.1007/s10712-009-9071-5).
- Roselli, P., N. Piana Agostinetti, and T. Braun, 2010, Shear-velocity and anisotropy structure of a retreating extensional forearc (Tuscany, Italy) from receiver functions inversion: *Geophysical Journal International*, **181**, 545–556, doi: [10.1111/j.1365-246X.2010.04520.x](https://doi.org/10.1111/j.1365-246X.2010.04520.x).
- Rothery, B. A., and W. E. A. Phillips, 1983, A report on the structures of the Clane Block: Prospecting License 1602, 5–10.
- Sambridge, M., 1999, Geophysical inversion with a neighbourhood algorithm—Part 1: Searching a parameter space: *Geophysical Journal International*, **138**, 479–494, doi: [10.1046/j.1365-246X.1999.00876.x](https://doi.org/10.1046/j.1365-246X.1999.00876.x).
- Savage, M. K., 1998, Lower crustal anisotropy or dipping boundaries? Effects on receiver functions and a case study in New Zealand: *Journal of Geophysical Research*, **103**, 69–78, doi: [10.1029/97JA02246](https://doi.org/10.1029/97JA02246).
- Savage, M., J. Park, and H. Todd, 2007, Velocity and anisotropy structure at the Hikurangi subduction margin, New Zealand from receiver functions: *Geophysical Journal International*, **168**, 1034–1050, doi: [10.1111/j.1365-246X.2006.03086.x](https://doi.org/10.1111/j.1365-246X.2006.03086.x).
- Schulte-Pelkum, V., and K. H. Mahan, 2014a, A method for mapping crustal deformation and anisotropy with receiver functions and first results from USArray: *Earth and Planetary Science Letters*, **402**, 221–233, doi: [10.1016/j.epsl.2014.01.050](https://doi.org/10.1016/j.epsl.2014.01.050).
- Schulte-Pelkum, V., and K. H. Mahan, 2014b, Imaging faults and shear zones using receiver functions: *Pure and Applied Geophysics*, **171**, 2967–2991, doi: [10.1007/s00240-014-0853-4](https://doi.org/10.1007/s00240-014-0853-4).
- Sebastopulo, G., and P. Wyse Jackson, 2009, Carboniferous: Mississippian (Tournaisian and Visean), in *The Geology of Ireland* (2nd ed.): Dunedin Academic Press, 215–268.
- Sherrington, H. F., G. Zandt, and A. Frederiksen, 2004, Crustal fabric in the Tibetan Plateau based on waveform inversion for seismic anisotropy parameters: *Journal of Geophysical Research*, **109**, doi: [10.1029/2002JB002345](https://doi.org/10.1029/2002JB002345).
- Shioi, K., and J. Park, 2008, Structural features of the subducting slab beneath the Kii Peninsula, central Japan: Seismic evidence of slab segmentation, dehydration, and anisotropy: *Journal of Geophysical Research*, **113**, 1–13, doi: [10.1029/2007JB005535](https://doi.org/10.1029/2007JB005535).
- Strogen, P., and I. D. Somerville, 1984, The stratigraphy of the Upper Palaeozoic Rocks of the Lyons Hill Area, County Kildare: *Irish Journal of Earth Sciences*, **6**, 155–173.
- Svenningsen, L., and B. H. Jacobsen, 2007, Absolute S-velocity estimation from receiver functions: *Geophysical Journal International*, **170**, 1089–1094, doi: [10.1111/j.1365-246X.2006.03505.x](https://doi.org/10.1111/j.1365-246X.2006.03505.x).
- Wessel, P., and W. H. F. Smith, 1998, New, improved version of generic mapping tool released: *Eos, Transactions American Geophysical Union*, **79**, 579–579, doi: [10.1029/98EO00426](https://doi.org/10.1029/98EO00426).
- Zevallos, I., M. Assumpção, and A. L. Padilha, 2009, Inversion of teleseismic receiver function and magnetotelluric sounding to determine basement depth in the Paraná Basin, SE Brazil: *Journal of Applied Geophysics*, **68**, 231–242, doi: [10.1016/j.jappgeo.2008.11.002](https://doi.org/10.1016/j.jappgeo.2008.11.002).
- Zheng, T., L. Zhao, and L. Chen, 2005, A detailed receiver function image of the sedimentary structure in the Bohai Bay Basin: *Physics of the Earth and Planetary Interiors*, **152**, 129–143, doi: [10.1016/j.pepi.2005.06.011](https://doi.org/10.1016/j.pepi.2005.06.011).
- Zhu, L., and H. Kanamori, 2000, Moho depth variation in southern California from teleseismic receiver function: *Journal of Geophysical Research*, **105**, 2969–2980, doi: [10.1029/1999JB900322](https://doi.org/10.1029/1999JB900322).